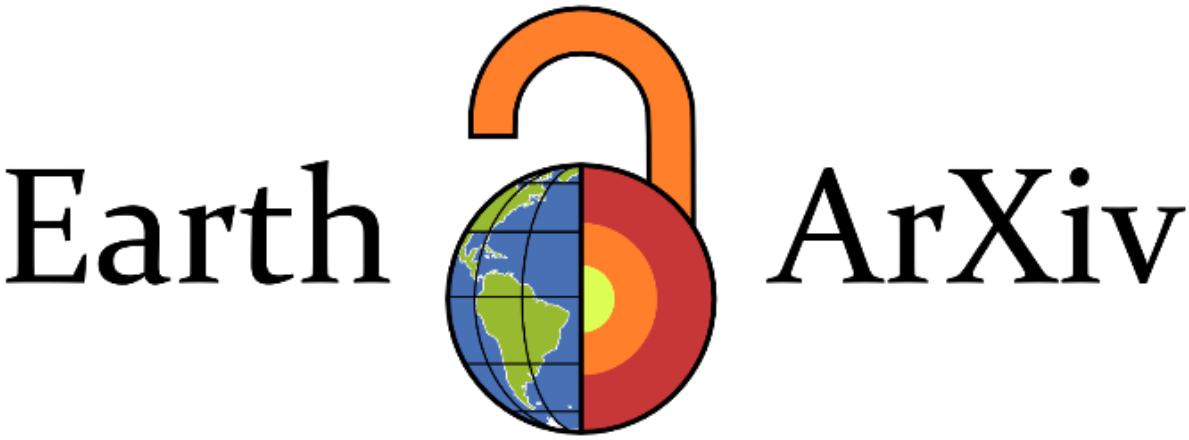

Cover Page

Manuscript Title:

Nanoindentation study of ripidolite and illite: Micromechanical controls on the sealing capacity of clay-rich caprocks

Authors' Names:

P. Cheng[1, *], T. Mishra[2], C.P. Zhang[3], J.M. Miocic[1]

[1] Energy and Sustainability Research Institute Groningen, University of Groningen, Nijenborgh 6, 9747 AG, Groningen, the Netherlands.

[2] Surface Technology and Tribology, Faculty of Engineering Technology, University of Twente, 7500 AE, Enschede, the Netherlands.

[3] State Key Laboratory of Coal Mine Disaster Dynamics and Control, School of Resources and Safety Engineering, Chongqing University, Chongqing, 400044, China.

***Corresponding Author:**

P. Cheng

Energy and Sustainability Research Institute Groningen, University of Groningen, Nijenborgh 6, 9747 AG, Groningen, the Netherlands.

Phone: +31 616 524 629

E-mail: p.cheng@rug.nl

Abstract

Clay-rich caprocks are essential for sealing underground energy storage formations, yet their micromechanical behavior under varying stress conditions is not well constrained. In particular, the influence of loading parameters on hardness, elastic modulus, fracture toughness, and time-dependent deformation of individual clay minerals remains insufficiently explored. This study addresses this gap through systematic nanoindentation experiments on ripidolite and illite, evaluating the effects of peak load, holding time, and loading rate on their mechanical response. Load-displacement curves revealed distinct behaviors: ripidolite frequently displayed pop-in events associated with localized plasticity, whereas illite deformed more smoothly. Across all conditions, illite showed shallower indentation depths, higher hardness, and higher elastic modulus, consistent with its stiffer microstructure and harder mineral inclusions. Ripidolite demonstrated a stronger indentation size effect in hardness and generally higher fracture toughness, indicating a greater ability to dissipate energy before crack propagation. Post-indentation imaging confirmed contrasting deformation modes, with ripidolite producing pronounced pile-up without visible cracking and illite showing limited pile-up but radial and lateral cracks. Creep tests revealed a two-stage response in both minerals; however, illite displayed higher creep ratios despite its greater strength, suggesting enhanced time-dependent deformation. Overall, these results highlight a fundamental trade-off: illite offers superior short-term resistance but is more vulnerable to brittle fracture and viscous strain, while ripidolite better resists crack growth but is more prone to immediate plastic deformation. Understanding such parameter-dependent behaviors improves predictions of caprock sealing performance under variable stress histories, informing risk assessments for subsurface energy storage operations.

Keywords*: Nanoindentation, Subsurface energy storage, Clay-rich caprock integrity, Hardness, Elastic modulus, Fracture toughness.*

1. Introduction

Clay minerals, a group of phyllosilicates with layered crystal structures, are among the most abundant constituents of fine-grained sedimentary rocks. Their structural units, tetrahedral and octahedral sheets, are bonded in various arrangements that govern their physical and chemical properties (Elmi, 2023). Owing to their abundance and low permeability, clay-rich rocks such as claystones, mudstones, and shales serve as key sealing formations in subsurface engineering applications, including underground hydrogen and carbon storage, hydrocarbon reservoirs, and waste isolation (Poda and Talal, 2025; Wethington et al., 2022).

The sealing capacity of such formations depends not only on their petrophysical properties but also on the geomechanical behavior of the constituent clay minerals. Processes such as compaction, fracture initiation, interlayer slip, and time-dependent creep can modify pore networks, thereby creating or closing fluid flow pathways that directly impact permeability and sealing efficiency (Dilshan et al., 2024). Assessing the micromechanical response of individual clay minerals is therefore essential to understand how local deformation mechanisms influence fluid migration and seal performance.

Traditional macroscale tests, such as triaxial compression, provide valuable data on the bulk elastic modulus and shear strength of clay-rich rocks (Ciancimino et al., 2024; Cosenza et al., 2023). For example, Ciancimino et al. (2024) reported a reduction in shear strength in a clayey caprock subjected to cyclic triaxial loading in the context of hydrogen storage. However, bulk tests average out the effects of mineral heterogeneity, grain contacts, and pore structures, masking the intrinsic response of individual minerals. Since sealing performance is strongly influenced by microscale deformation processes at grain boundaries and contact interfaces, methods capable of probing local properties are needed.

Nanoindentation provides such an approach, measuring hardness, elastic modulus, and fracture toughness at submicron scales (Cheng et al., 2022; Mu et al., 2024). By probing

localized regions, nanoindentation captures mineral-scale plasticity, crack initiation, and creep that are not accessible through bulk tests. This is particularly important for clay-rich formations, where sealing behavior depends on microstructural heterogeneity and the mechanical response of individual phyllosilicate grains. Previous studies have applied nanoindentation to clay-rich rocks, including claystones (Bartier and Auvray, 2017) and shales (Ma et al., 2025; Wang et al., 2023), to extract mechanical properties of constituent clays in situ. However, interpretations are often complicated by matrix effects from surrounding minerals and pores (Shi et al., 2024). Investigations on single phyllosilicate minerals offer clearer insights into structure-property relationships. For example, Mukherjee and Misra (2023) related variations in mechanical response to interlayer cations and electrostatic interactions, while Zhang et al. (2013) demonstrated that the type and strength of interlayer interaction govern deformation mechanisms across different phyllosilicates.

Among clay minerals, ripidolite (a chlorite) and illite are especially relevant to sealing performance. Both occur widely in clay-rich caprocks and contribute to low-permeability barriers, but they represent contrasting structural types. Ripidolite has a 2:1:1 layer structure with interlayer hydroxide sheets, while illite possesses a 2:1 structure stabilized by potassium ions in the interlayer (Konta, 2009). These structural differences control their ability to undergo plastic deformation, initiate fractures, and maintain dimensional stability under subsurface stresses. Illite commonly occupies grain boundaries in sealing rocks and enhances fine-grained matrix compaction, whereas chlorite, including ripidolite, can influence sealing through its reactivity and role in mineral transformations during fluid-rock interactions (Dje and Radonjic, 2025; Yang et al., 2020). Despite their prevalence and functional significance, systematic nanoindentation studies on ripidolite and illite as single minerals remain scarce, leaving a gap in understanding how their intrinsic micromechanical properties influence sealing integrity.

This study performs systematic nanoindentation tests on ripidolite and illite to evaluate the effects of peak load, holding time, and loading rate on their hardness, elastic modulus, fracture toughness, and creep behavior. These parameters were chosen to simulate key subsurface conditions: peak load reflects stresses induced by pore pressure buildup, holding time represents sustained loading relevant to long-term storage, and loading rate captures the effect of injection or withdrawal dynamics (Bennett et al., 2015). Post-indentation morphologies are further analyzed to link micromechanical parameters with deformation mechanisms. The results provide insights into how intrinsic mineral properties and loading conditions interact to control deformation and fracture at the microscale, with direct implications for evaluating the sealing capacity of clay-rich formations in subsurface energy storage.

2. Materials and methods

2.1.Sample selection and preparation

Two clay mineral samples were obtained from The Clay Minerals Society: ripidolite (CCa-2 reference code) and illite (IMt-2 reference code). Their major chemical compositions, shown in Table 1, highlight differences in silica, alumina, and iron contents. As these are naturally sourced materials, they contain varying amounts of mineral impurities. The types and quantities of impurities, which influence mechanical behavior, are listed in Table 2 based on previous mineralogical studies (Gailhanou et al., 2007; Vogt et al., 2002).

For nanoindentation, small chips of each clay mineral were embedded in epoxy resin to create solid mounts. A multi-step grinding and polishing procedure was used to achieve smooth and flat surfaces suitable for indentation. Initial grinding employed 54 μm and 20 μm grit size diamond abrasives, followed by polishing with 9 μm and 2 μm grit size alumina oxide abrasives. Final polishing was completed using 1 μm and 0.05 μm alcohol-based suspensions to minimize surface damage. Throughout this process, water was avoided as a lubricant to prevent clay swelling and preserve surface integrity.

Table 1 Major chemical compositions (wt%) of ripidolite (CCa-2) and illite (IMt-2) reference samples (The Clay Minerals Society).

Mineral code	SiO_2	Al_2O_3	TiO_2	Fe_2O_3	FeO	MnO	MgO	CaO	Na_2O	K_2O	P_2O_5
CCa-2	26.00	20.00	0.476	26.60	20.80	0.10	17.20	0.25	< 0.10	< 0.10	0.02
IMt-2	49.30	24.25	0.55	7.32	0.55	0.03	2.56	0.43	0	7.83	0.08

Table 2 Identified mineral impurities (wt%) in ripidolite and illite (Gailhanou et al., 2007; Vogt et al., 2002). n.d. = not detected.

Mineral code	Quartz	Kaolinite	Microcline	Illite/mixed layer	Chlorite	Rutile
CCa-2	n.d.	n.d.	n.d.	8.80	n.d.	n.d.
IMt-2	7.50	0.30	2.00	n.d.	traces	0.87

Cylindrical specimens approximately 10 mm in height and 20 mm in diameter were prepared for each mineral. Surface roughness of the polished samples was then assessed using a Sensofar confocal microscope at 20× magnification, with at least three measurements performed per sample to ensure accuracy. Each measurement covered an area of 877.20 × 660.48 μm^2, which provided a sufficiently large and representative region for subsequent indentation tests. The measured root mean square roughness (R_q) and arithmetic mean roughness (R_a) values are presented in Table 3. Illite exhibited higher surface roughness than ripidolite, likely due to its greater mineral heterogeneity and higher impurity content, which hinder polishing to a smoother finish.

Table 3 Surface roughness (in μm) of ripidolite and illite.

	CCa-2	IMt-2
R_q	0.309 ± 0.026	0.508 ± 0.082
R_a	0.242 ± 0.019	0.384 ± 0.054

2.2.Nanoindentation technique

2.2.1. Instrumentation

Nanoindentation tests were conducted using an Anton Paar NHT^2 Nanoindenter equipped with a Berkovich diamond tip. The depth-sensing indentation technique in the Nanoindenter records force and displacement continuously during loading, holding, and unloading, enabling

the determination of key mechanical properties such as hardness and elastic modulus (Fischer-Cripps, 2007). The system uses a piezo-electric actuator to apply load and a capacitive sensor to measure displacement, with a load range of 0.1-500 mN at a resolution of 0.02 µN, loading rates of 0.1-10 N/min, and penetration depths of 40-200 µm at a resolution of 0.01 nm. A schematic of the nanoindentation system, indenter geometry, and representative load-displacement curve is shown in Fig. 1.

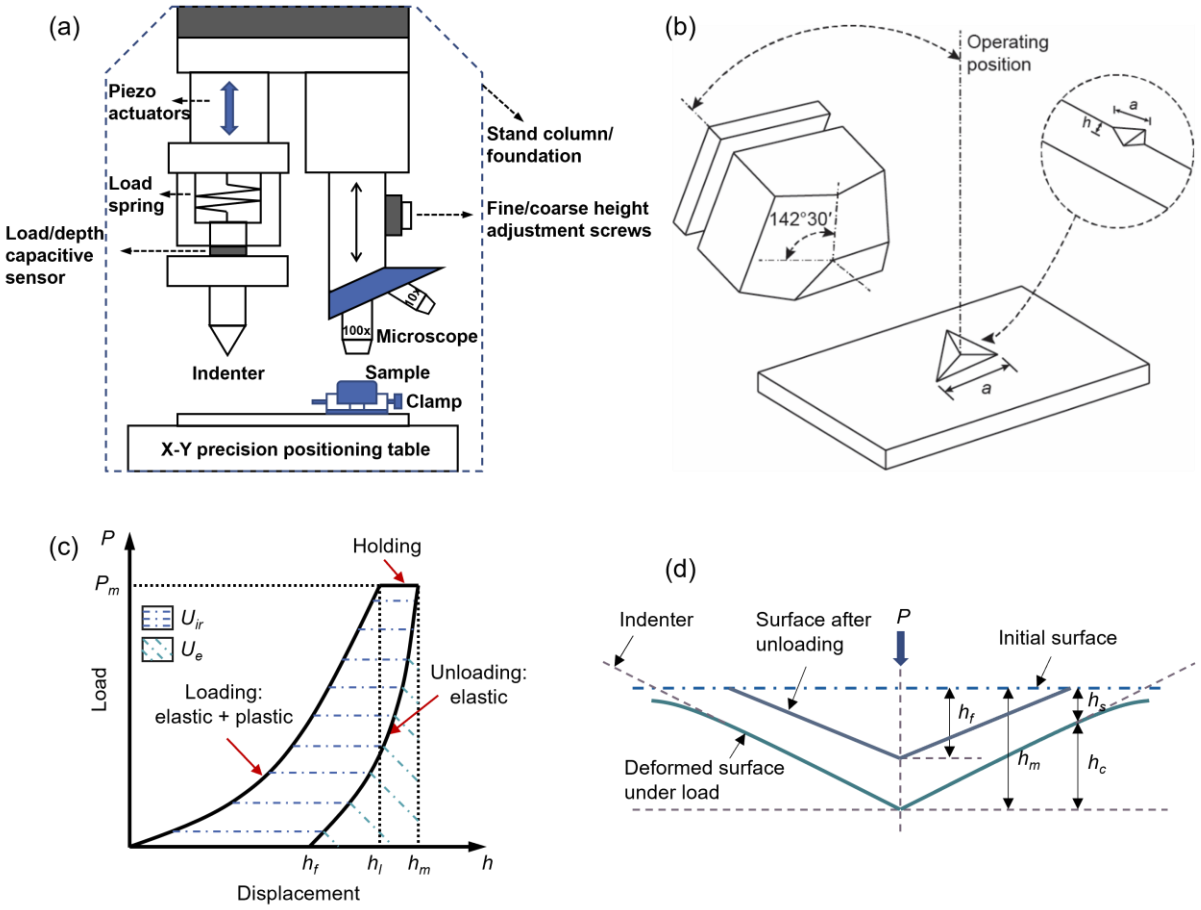

Fig. 1 (a) Schematic diagram of the nanoindentation system; (b) illustration of the Berkovich tip geometry and indentation imprint (adapted from Mishra et al. (2020)); (c) representative load-displacement curve (described in Section 2.2.3); (d) diagram of the indentation zone with key parameters: h_s = surface displacement at the contact perimeter; h_f = final indentation depth.

2.2.2. Testing protocol

Indentations were arranged in 3×3 or 2×3 grids for ripidolite and illite to enable statistical analysis of the mechanical properties. To minimize interaction effects between adjacent indents

and ensure the reliability of the results, individual indents within each grid were spaced 100 µm apart, while a distance of 200 µm was maintained between separate grids.

To investigate the influence of indentation parameters on the mechanical response, three sets of tests were conducted by varying the following test parameters:

a) Peak load: Indentations were performed at peak loads of 20, 60, 120, 160, and 200 mN with a constant loading and unloading rate of 200 mN/min and a holding time of 5 s at maximum load. These tests were conducted to investigate load dependence and to specifically evaluate the potential indentation size effect (ISE) on hardness.

b) Holding time: At a fixed peak load of 120 mN and a constant loading/unloading rate of 200 mN/min, holding times of 5, 10, and 20 s were applied. These experiments were intended to explore the time-dependent deformation of the clay minerals and assess their potential creep behavior.

c) Loading rate: To evaluate the rate-dependent sensitivity, loading rates of 150, 200, and 300 mN/min were applied while maintaining a peak load of 120 mN and a holding time of 5 s.

2.2.3. Analysis procedure

A typical nanoindentation test consists of a linearly increasing loading phase, followed by a short holding period, and then a linearly decreasing unloading phase. Throughout this process, a load-displacement (*P*-*h*) curve is recorded, from which the mechanical properties of the material can be derived (Fig. 1 (c)). The loading phase captures both the initial elastic and subsequent plastic deformation, while the unloading phase reflects purely elastic recovery.

The constant loading rate nanoindentation method, commonly referred to as quasi-static nanoindentation, operates based on principles extensively reviewed by Oliver and Pharr (1992). Using the *P*-*h* curve obtained during testing, key mechanical properties of the material can be

extracted through the well-established Oliver-Pharr (O-P) method, which remains a standard approach in nanoindentation analysis.

Hardness (H) is calculated as the peak load divided by the contact area:

$$H = \frac{P_m}{A_c} \tag{1}$$

where A_c is the contact area and P_m is the peak load. The contact area for nanoindentation using a Berkovich indenter is calculated as:

$$A_c = 24.5 h_c^2 \tag{2}$$

where h_c is the contact depth (Fig. 1 (d)). The contact depth is given by:

$$h_c = h_m - 0.75 \times \frac{P_m}{S} \tag{3}$$

where h_m is the maximum indentation depth, S is the contact stiffness, which is obtained from the slope of the initial portion of the unloading curve:

$$S = \frac{dP}{dh} \tag{4}$$

The reduced elastic modulus E_r is calculated as:

$$E_r = \frac{\sqrt{\pi} S}{2\beta\sqrt{A_c}} \tag{5}$$

where β is a constant dependent on the indenter geometry (1.034 for a Berkovich indenter).

Finally, the elastic modulus of the sample is derived from the following relationship:

$$\frac{1}{E_r} = \frac{1-\nu^2}{E} + \frac{1-\nu_i^2}{E_i} \tag{6}$$

where E is the elastic modulus and ν is the Poisson's ratio of the sample, while E_i and ν_i are those of the diamond indenter. For a Berkovich indenter, E_i = 1140 GPa and ν_i = 0.07. According to Cosenza et al. (2023), the Poisson's ratios used in this study are 0.36 and 0.31 for ripidolite and illite, respectively.

The energy method was employed to evaluate the fracture toughness of the clay samples. As illustrated in Fig. 1 (c), the total energy (U_t) involved in the nanoindentation process can be partitioned into elastic energy (U_e), pure plastic energy (U_{pp}), and fracture energy (U_f). Both the U_t and the U_e were derived directly from the *P*-*h* curves. The irreversible energy (U_{ir}), which represents the energy not recovered upon unloading, was calculated as the difference between U_t and U_e (Cheng et al., 2002). A key assumption in this analysis is that no significant energy is lost at the indenter-sample interface; thus, the U_{ir} is entirely dissipated through plastic deformation and crack formation. Accordingly, the U_f of cracks is obtained by:

$$U_f = U_{ir} - U_{pp} = U_t - U_e - U_{pp} \tag{7}$$

The loading and the unloading segments of the indentation curve are typically modeled using power-law functions (Liu et al., 2016):

$$P = P_m \frac{h^n}{h_l^n} = Kh^n, \text{ loading} \tag{8}$$

$$P = P_m \frac{(h-h_f)^m}{(h_m-h_f)^m} = \alpha(h-h_f)^m, \text{ unloading} \tag{9}$$

Using these fitted expressions, the U_e and U_t can be calculated as:

$$U_e = \int_{h_f}^{h_m} \alpha(h-h_f)^m dh = \frac{P_m(h_m-h_f)}{1+m} \tag{10}$$

$$U_t = \int_0^{h_l} Kh^n dh + \int_{h_l}^{h_m} P_m dh = \frac{P_m h_l}{1+n} + P_m(h_m-h_l) \tag{11}$$

where h_l is the displacement at the beginning of the holding segment, and *K*, α, *n*, and *m* are the fitting coefficients obtained from curve fitting.

For an ideal elastoplastic material in which no fracture occurs, the relationship between U_{pp} and U_t is defined as (Zeng et al., 2017):

$$\frac{U_{pp}}{U_t} = 1 - \frac{U_e}{U_t} = 1 - \frac{(1+n)(1-\frac{h_f}{h_m})}{(1+m)(1+n-n\frac{h_f}{h_m})} \quad (12)$$

The critical energy release rate (G_c), defined as the energy released per unit area of the crack plane, is expressed as:

$$G_c = \frac{\partial U_f}{\partial A} = \frac{U_f}{A_m} \quad (13)$$

where A_m is the maximum crack area. For a Berkovich indenter, this area can be estimated as:

$$A_m = 24.5h_m^2 \quad (14)$$

Thus, the fracture toughness of the material can be determined using the following expression:

$$K_c = \sqrt{G_c E_r} \quad (15)$$

2.3.Microstructural characterization

After nanoindentation testing, each indent was imaged using the system's integrated optical microscope at 100× magnification. To obtain a more detailed view of the surface topography, the clay samples were further examined using a Sensofar confocal microscope at 150× magnification. This approach enabled the acquisition of high-resolution three-dimensional (3D) surface profiles for ripidolite and illite. These 3D images provided quantitative measurements of residual depths and pile-up heights, complementing the nanoindentation data with direct observations of deformation features.

3. Results

3.1.*P-h* curves

Before analysis, a filtering step was applied to improve data reliability. Due to mineral impurities and surface heterogeneity, indentation curves showing significant deviations under identical test conditions were excluded. Optical microscopy images of the indents also helped

identify and eliminate abnormal cases. After this selection, one representative curve was chosen for each test condition and each mineral and is presented in Fig. 2.

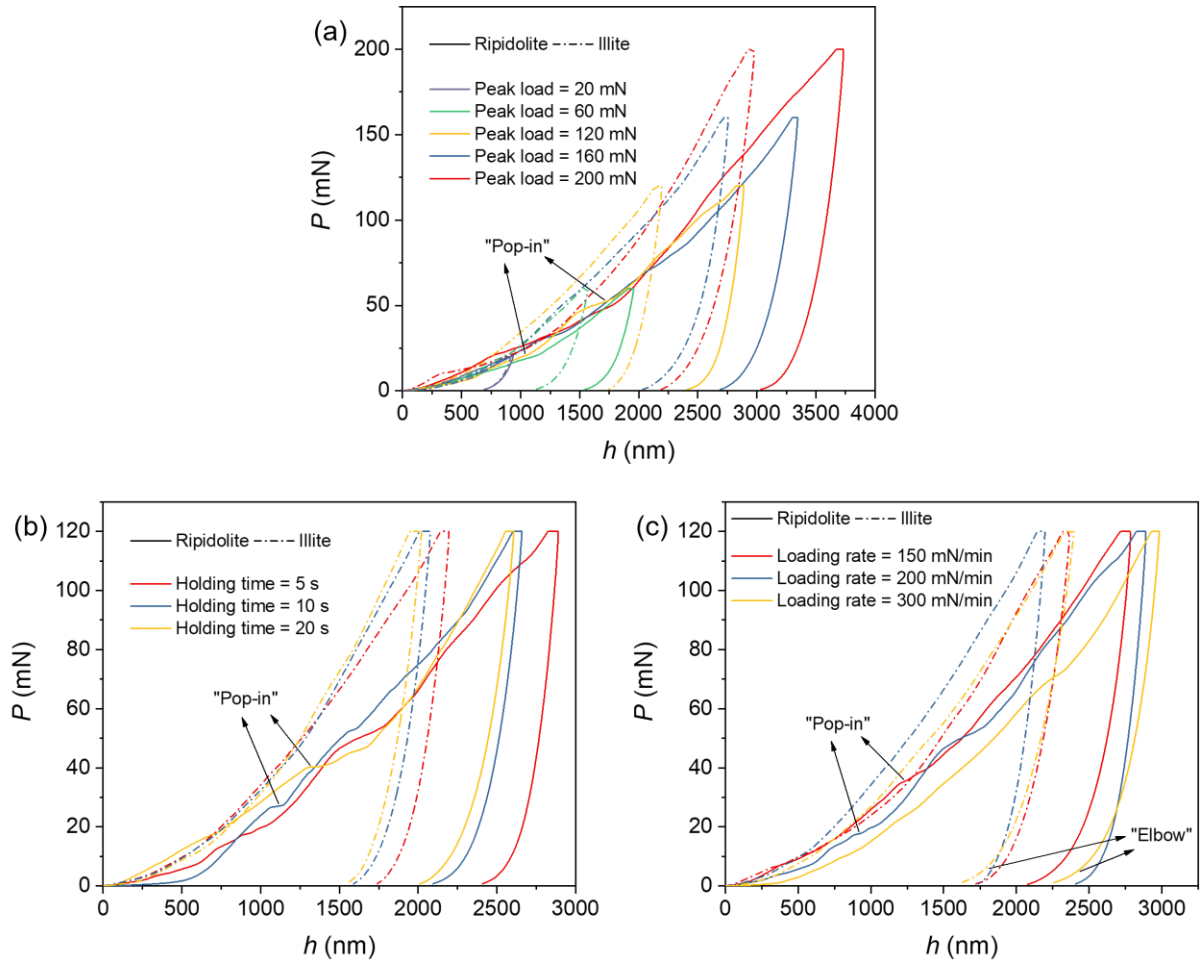

Fig. 2 Representative *P*-*h* curves for ripidolite and illite under different (a) peak loads, (b) holding times, and (c) loading rates.

In Fig. 2 (a), indentation depth increases with peak load for both ripidolite and illite. At 20 mN, their *P*-*h* curves are similar. However, with increasing load, the curves diverge, reflecting their structural differences. In all cases, the rate of depth increase slows as peak load rises, indicating a reduced incremental penetration response. The loading curves of ripidolite frequently display abrupt displacement steps, commonly referred to as “pop-in” events. These occur when the material suddenly undergoes localized plastic deformation, typically due to the dislocation nucleation or pore collapse (Ohmura and Wakeda, 2021). In contrast, illite shows smoother loading curves with no noticeable discontinuities, indicating more uniform

deformation. The frequent pop-ins in ripidolite are likely associated with its more porous and heterogeneous microstructure, as confirmed by optical imaging.

According to Fig. 2 (b), pop-in persists in ripidolite across various holding times, while illite maintains a stable response. Interestingly, increasing holding time from 5 to 20 s shifts the curves slightly leftward, indicating reduced indentation depth. This effect may be attributed to the short holding times used here, which are insufficient to fully capture time-dependent deformation, leaving results more sensitive to local heterogeneity in minerals. Fig. 2 (c) shows that ripidolite again exhibits multiple pop-ins across different loading rates. In addition, another feature becomes apparent in the unloading portion of the curves. A sharp change in slope, known as an “elbow”, is observed, especially at the highest unloading rate of 300 mN/min. This reflects a viscoelastic response in the material, where elastic recovery occurs slower than the indenter retraction. As a result, the indenter partially loses contact during unloading, producing the characteristic elbow shape in the curve (Domnich et al., 2000).

3.2.Indentation depth

Fig. 3 presents the final indentation depth (h_f) and maximum indentation depth (h_m) for ripidolite and illite under varying test conditions. These parameters provide a quantitative comparison of their mechanical responses. In all cases, illite shows smaller indentation depths than ripidolite, indicating its greater resistance to deformation and thus higher mechanical strength. Despite this difference in magnitude, both minerals follow similar trends in how h_f and h_m respond to changes in test parameters.

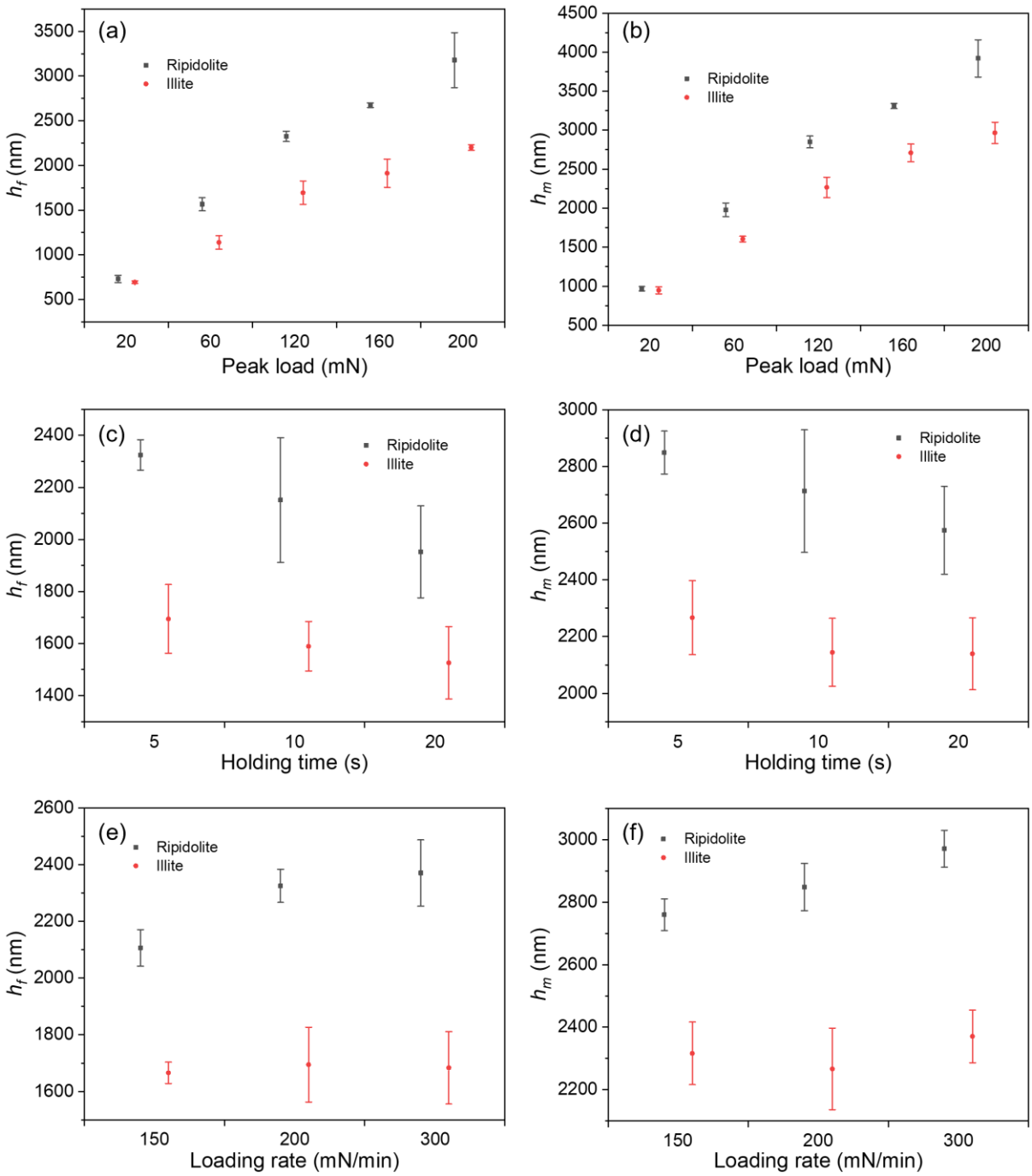

Fig. 3 Final indentation depth ((a), (c), and (e)) and maximum indentation depth ((b), (d), and (f)) for ripidolite and illite under different test conditions: varying peak load, holding time, and loading rate.

As shown in Fig. 3 (a) and (b), h_f and h_m increase with increasing peak load in both minerals, with divergence more pronounced at higher loads. For example, the mean h_f of ripidolite increases from 729.76 nm at 20 mN to 3178.22 nm at 200 mN, representing an increase by a factor of 3.36. In comparison, illite shows a more moderate rise from 694.17 nm to 2200.52 nm, corresponding to an increase by a factor of 2.17. These results indicate that ripidolite is

more susceptible to deformation under higher loads, while illite is more mechanically stable. Fig. 3 (c) and (d) show that both h_f and h_m decrease slightly with longer holding times, more strongly in ripidolite than in illite. While this reduction may indicate time-dependent recovery processes such as viscoelastic relaxation (Chudoba and Richter, 2001), the short holding durations applied here restrict firm conclusions. The stronger response in ripidolite is likely related to its more porous and structurally weaker framework, which is more sensitive to local variations. In Fig. 3 (e) and (f), an increase in loading rate results in a substantial rise in both h_f and h_m for ripidolite, whereas illite shows only minor changes. This behavior indicates that plastic deformation dominates the rate dependence in ripidolite. At slower loading rates, ripidolite can redistribute stress through microstructural adjustments such as interlayer slip or pore collapse, limiting penetration depth. At faster loading rates, these relaxation processes are suppressed, and the applied stress is more directly converted into localized plastic deformation, resulting in deeper indents. The rigid framework of illite, reinforced by inclusions, shows little sensitivity to rate changes.

3.3.Post-indentation microstructure

With the use of optical microscopy and confocal microscopy, both 2D images and 3D surface topographies of the indentations were obtained. Fig. 4 presents optical images, 3D surface maps, and corresponding altitude profiles of ripidolite subjected to indentation at representative peak loads of 20, 120, and 200 mN.

From these images (Fig. 4), visible pores can be observed near the indentations. These pre-existing surface features are likely responsible for the pop-ins identified in the loading segments of the *P-h* curves for ripidolite. In addition, pile-up is clearly evident under all three peak load conditions, indicating that material around the indent has plastically displaced outward. This behavior implies localized plastic flow at the contact boundaries and is consistent with observations reported for elastic-plastic materials under nanoindentation (Ma et al., 2024).

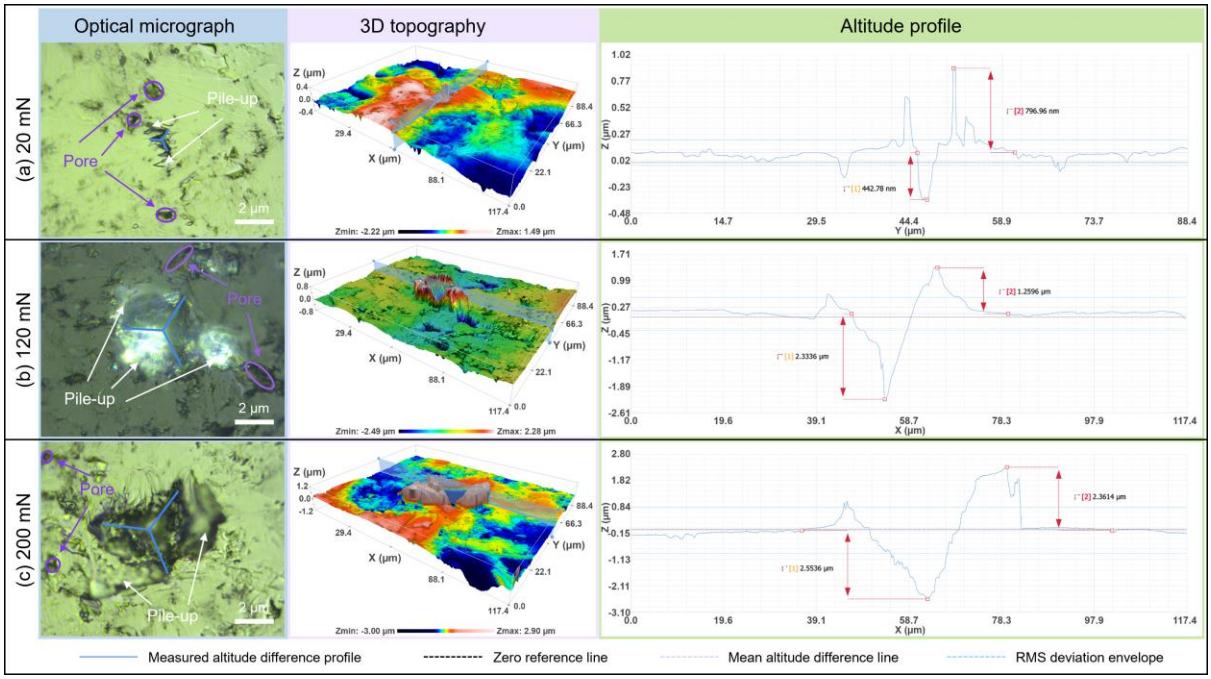

Fig. 4 Optical micrographs, 3D topographies, and altitude profiles of indents on ripidolite at peak loads of (a) 20 mN, (b) 120 mN, and (c) 200 mN.

At 20 mN, the imprint appears smallest in size, with a residual indentation depth of about 0.44 μm and a pile-up height of about 0.80 μm. At 120 mN, the imprint becomes larger, with a residual indentation depth of 2.33 μm and a pile-up height of 1.26 μm. At 200 mN, the largest imprint is observed, corresponding to the greatest residual indentation depth and pile-up height, measured at 2.55 μm and 2.36 μm, respectively. When these residual depths are compared with the h_f reported in Fig. 3 (a), which are 0.73 ± 0.04 μm, 2.32 ± 0.06 μm, and 3.18 ± 0.31 μm at 20, 120 and 200 mN respectively, the values at 120 mN show good agreement. However, at 20 and 200 mN, the residual depths measured from 3D profiles are lower than the instrumented nanoindentation results. At low load, this difference likely reflects the influence of surface roughness, as the indentation size is comparable to the scale of surface asperities. At high load, elastic recovery is less likely to dominate the response, and variability in local surface heterogeneity provides a more plausible explanation for the reduced residual depth.

Fig. 5 shows corresponding data for illite. Unlike ripidolite, illite exhibits fewer visible surface pores, although the optical images reveal the presence of distinct mineral grains, suggesting that illite is mixed with mineral impurities of different compositions.

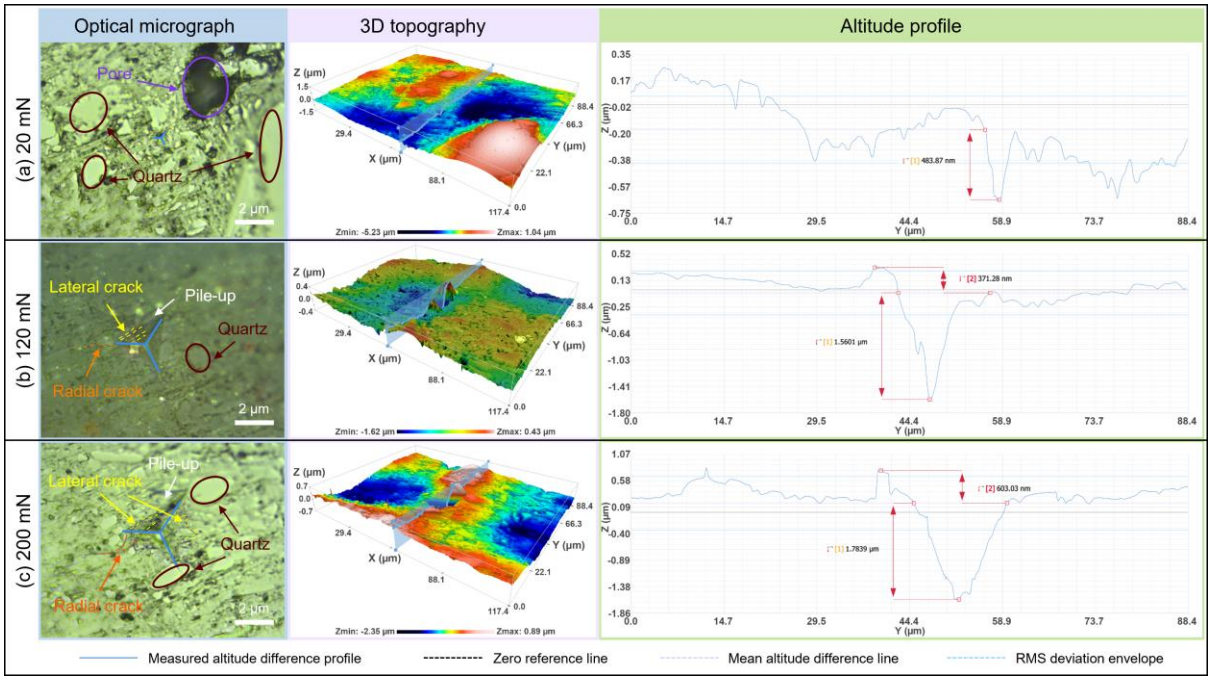

Fig. 5 Optical micrographs, 3D topographies, and altitude profiles of indents on illite at peak loads of (a) 20 mN, (b) 120 mN, and (c) 200 mN.

Pile-up in illite is less prominent under all loading conditions, and the indentation sizes are generally smaller than those in ripidolite under the same loading. At 20 mN, the residual indentation depth is approximately 0.48 μm, with no detectable pile-up around the indent. At 120 mN, the residual indentation depth increases to 1.56 μm, and a small pile-up of 0.37 μm is observed. At 200 mN, the residual indentation depth reaches 1.78 μm, accompanied by a pile-up of 0.60 μm. Additionally, optical images show the presence of both radial and lateral cracks at 120 and 200 mN. Radial cracks are typically caused by tensile stresses generated during unloading, while lateral cracks are associated with shear-induced damage during loading (Chen et al., 2005). These cracking patterns are commonly observed in brittle materials under concentrated loading and have also been reported in previous nanoindentation studies (Kulshreshtha et al., 2012).

Compared with the h_f values from Fig. 3 (a), which are measured as 0.69 ± 0.01 μm, 1.69 ± 0.13 μm, and 2.20 ± 0.03 μm for 20, 120 and 200 mN respectively, the 120 mN condition again shows good consistency. At 20 and 200 mN, the residual depths are lower than the instrumented indentation values, a discrepancy consistent with that observed in ripidolite and likely arising from surface roughness at low load and local surface heterogeneity at high load.

In terms of residual depth, illite and ripidolite are comparable at 20 mN. However, at 120 and 200 mN, illite exhibits significantly lower depths, consistent with Fig. 3 (a) and indicating greater resistance to penetration under increasing load. The pile-up behavior shows an even clearer distinction: ripidolite develops markedly higher pile-up than illite under the same conditions. This contrast demonstrates differences in deformation mechanisms. Optical images confirm that ripidolite undergoes substantial outward material flow with no visible cracking, whereas illite displays limited pile-up but visible radial and lateral cracks. These differences can be attributed to their microstructures. Ripidolite's porous and structurally weaker matrix favors plastic flow and interlayer bending, producing pile-up. Illite, by contrast, is reinforced by harder mineral inclusions such as quartz, which enhance its stiffness, restrict plastic deformation, and promote brittle fracture.

Because ripidolite and illite did not exhibit distinct indentation imprints under the holding time or loading rate conditions applied in this study, it was deemed unnecessary to present and compare their corresponding images for these test variables.

4. Discussion

4.1. Variations in *H* and *E*

To examine the influence of loading parameters on *H* and *E* of the two clay minerals, bar charts were constructed as shown in Fig. 6. Across all loading conditions, ripidolite consistently exhibits lower *H* and *E* values than illite, with the difference particularly pronounced for *H*. For example, at a peak load of 120 mN with a holding time of 5 s and a loading rate of 200

mN/min, the mean *H* values are 0.62 GPa for ripidolite and 1.02 GPa for illite, whereas the corresponding mean *E* values are 41.21 GPa and 46.53 GPa, respectively. This distinction can be attributed to fundamental differences in microstructure, porosity, and mineral composition between the two clays. Ripidolite is characterized by a higher degree of structural porosity and a composition that promotes greater plastic deformation under load. Both minerals share a 2:1 layered structure, as shown in Fig. 7, but ripidolite belongs to the chlorite group and features an additional brucite-like hydroxide sheet between adjacent layers, forming a 2:1:1 configuration. This interlayer may facilitate layer bending or shearing during indentation (Pauling, 1930). In contrast, the 2:1 layers in illite are held together by interlayer potassium ions, which rigidly fix the layers and inhibit interlayer movement (Stixrude and Peacor, 2002). Moreover, illite also includes harder mineral impurities such as quartz, contributing to its greater mechanical resistance. These structural and compositional features result in illite exhibiting higher *H* and *E* values, while ripidolite shows greater susceptibility to localized plastic deformation.

As shown in Fig. 6 (a), the *H* of ripidolite decreases with increasing peak load. This decline is particularly evident between 20 and 60 mN, where the mean *H* drops from 0.85 GPa to 0.64 GPa. Such behavior is indicative of the indentation size effect (ISE), a phenomenon in which hardness decreases as indentation load or depth increases, especially near the surface of the material (Ma et al., 2021).This effect is amplified in ripidolite due to its higher porosity, which promotes localized plastic deformation under larger loads. In contrast, the *E* of ripidolite shows no consistent trend with increasing load. For illite, neither *H* nor *E* demonstrates a systematic dependence on peak load, suggesting that the ISE is not significant for this mineral under the tested conditions.

Fig. 6 (b) illustrates that *H* increases with longer holding durations for both minerals, while *E* remains relatively stable. This trend indicates that some degree of time-dependent relaxation

or recovery occurs during the holding segment, reducing the indentation depth (as shown in Fig. 3) and thereby increasing the measured *H*. Such effects likely reflect viscoelastic or viscoplastic responses at the microscale (Chudoba and Richter, 2001). The stability of *E* values across different holding times suggests that the elastic behavior is unaffected by the duration of the hold segment.

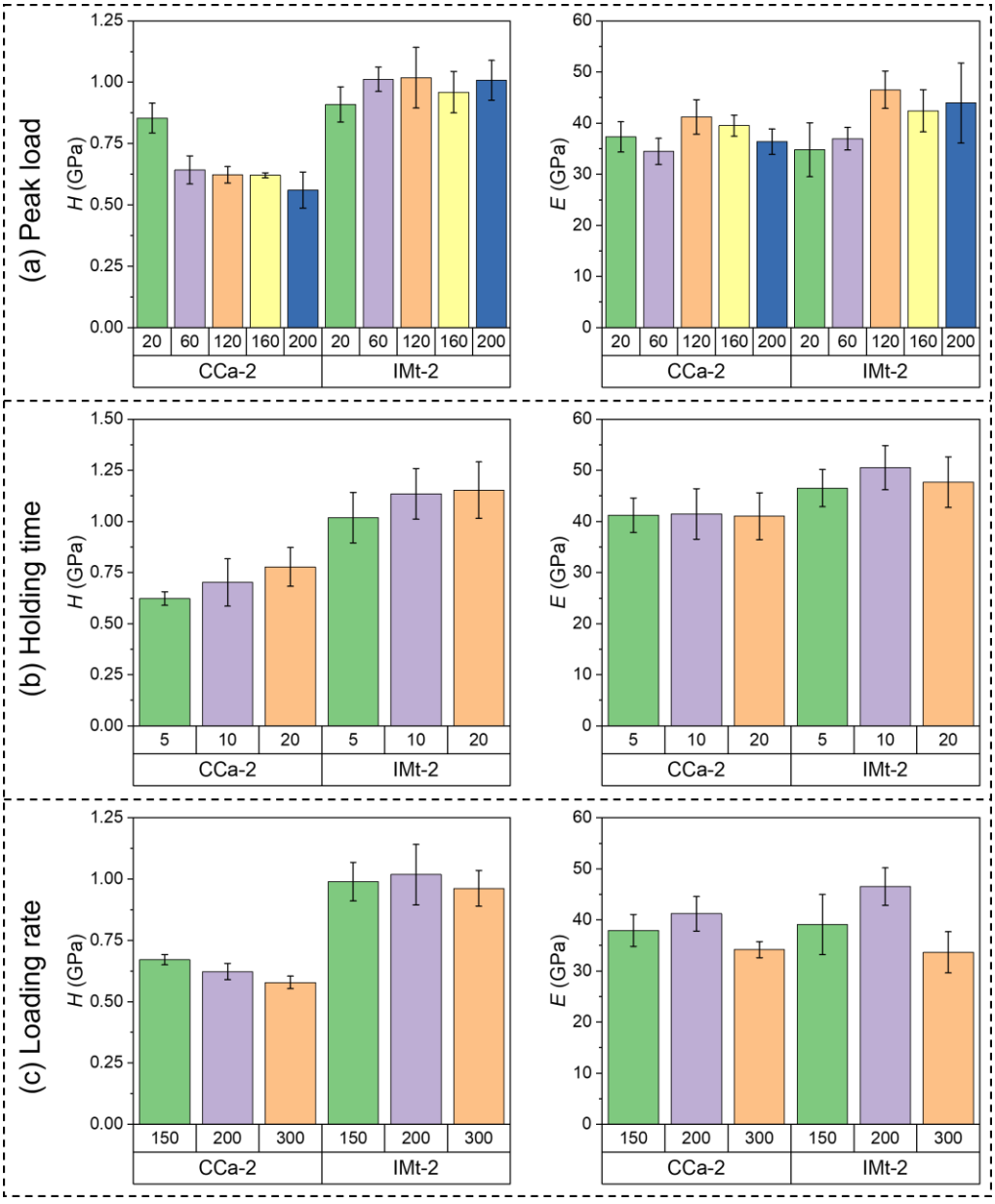

Fig. 6 Variations in *H* and *E* for ripidolite and illite under different (a) peak loads, (b) holding times, and (c) loading rates.

In Fig. 6 (c), H of ripidolite decreases as the loading rate increases, whereas illite shows no clear trend. In terms of E, neither mineral exhibits a consistent response to changes in loading rate. The decline in hardness for ripidolite is consistent with the corresponding increase in indentation depth at higher rates, indicating that rapid loading promotes more localized plastic deformation and deeper penetration. This response demonstrates the greater sensitivity in ripidolite's porous and mechanically weaker structure to loading dynamics. In contrast, the more rigid framework of illite shows limited rate dependence under the tested conditions.

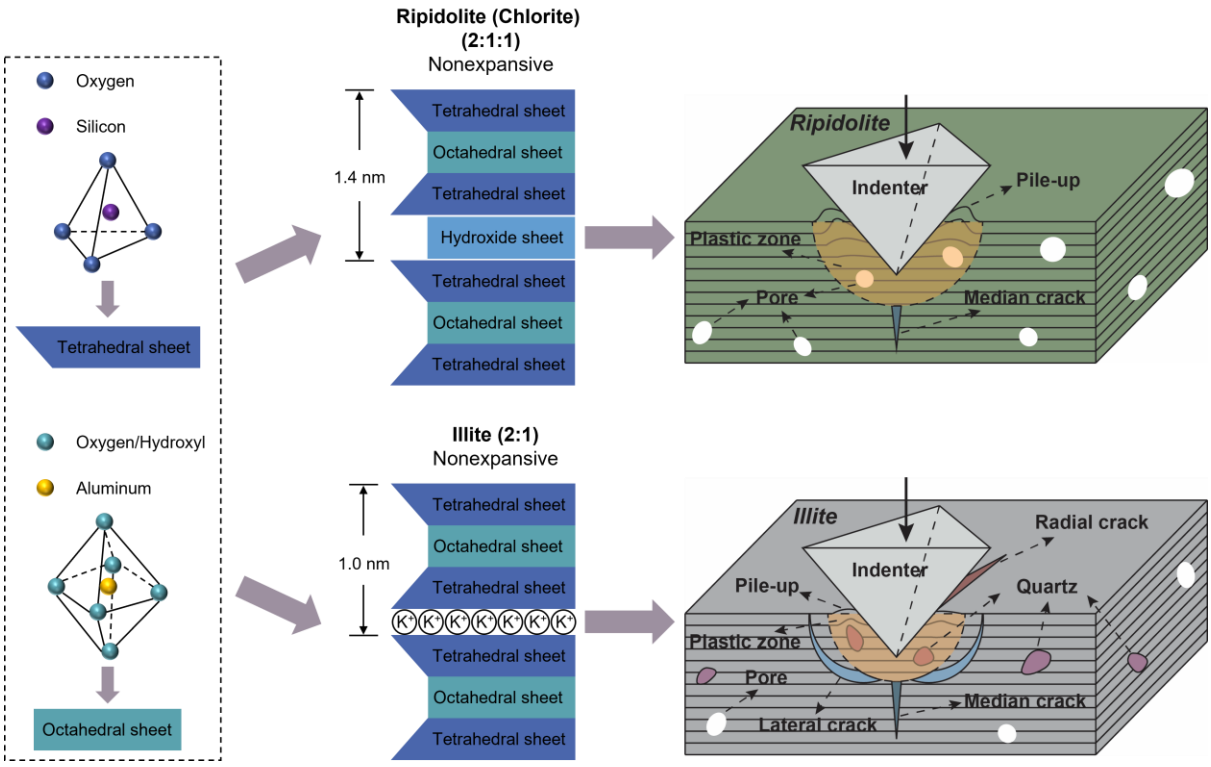

Fig. 7 Schematic illustration of the structural characteristics of ripidolite and illite and their dominant mechanical responses under nanoindentation.

4.2.Variations in K_c

Fracture toughness of ripidolite and illite was determined using the energy method. The loading and unloading segments of the P-h curves were fitted with Eqs. (8) and (9), and the resulting fitting coefficients n and m, the reduced modulus (E_r) and energy components (U_e, U_t, and U_f), are summarized in Table 4. These values were then applied in Eq. (15) to calculate K_c at various peak loads, as presented in Fig. 8 (a). It is important to note that certain P-h curves

exhibiting pronounced pop-ins could not be satisfactorily fitted and were therefore excluded from the analysis.

Table 4 Summary of nanoindentation parameters used in fracture toughness calculations for ripidolite and illite.

Mineral	No.	P_m (mN)	n	m	E_r (GPa)	U_e (pJ)	U_t (pJ)	U_f (pJ)
Ripidolite	1	20	1.567	4.960	39.064	1639.668	7843.122	167.829
	2	20	1.459	4.523	38.864	1648.530	8161.380	230.047
	3	20	1.621	4.159	41.613	1461.721	7744.720	35.715
	4	60	1.885	3.862	37.205	7221.367	43186.680	1497.410
	5	60	1.787	3.717	42.310	6612.720	41814.055	714.906
	6	120	1.549	4.401	46.247	15886.594	145161.266	3503.148
	7	120	1.904	3.908	42.949	16525.246	130619.484	6256.615
	8	120	1.662	3.811	47.593	14690.109	135630.891	1343.346
	9	120	1.557	3.982	39.085	19112.688	145379.016	2876.298
	10	160	1.905	3.748	42.718	26204.547	188476.766	1799.948
	11	160	1.416	3.825	45.390	25264.785	229736.156	6687.201
	12	200	1.772	3.814	42.864	36707.824	287963.906	12892.236
	13	200	1.544	3.772	39.945	35350.789	330657.438	4279.559
Illite	1	20	2.199	3.738	38.727	1550.081	6383.299	191.534
	2	20	2.432	4.413	41.774	1551.833	5746.459	129.521
	3	60	1.682	3.413	38.345	8325.710	38478.867	854.390
	4	60	1.895	3.659	42.347	7959.652	34381.734	332.486
	5	60	1.658	3.566	42.048	7275.004	38851.785	262.650
	6	120	1.742	3.274	48.779	19281.889	98712.367	2596.570
	7	120	1.635	3.959	51.793	17383.584	115945.859	785.401
	8	120	1.702	3.695	46.794	20464.170	102702.977	1775.650
	9	160	1.469	3.594	45.166	33908.395	171382.766	1428.810
	10	160	1.852	3.599	39.090	34582.086	164084.875	1476.894
	11	200	2.115	3.731	43.965	44808.984	205135.875	9118.721
	12	200	1.603	3.821	40.282	47922.543	242527.484	1135.514

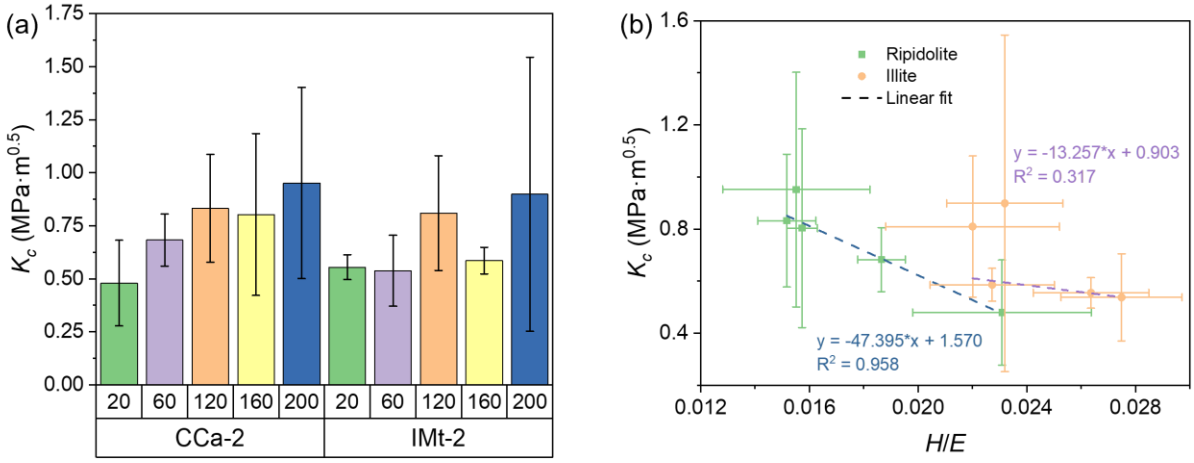

Fig. 8 (a) K_c of ripidolite and illite at different peak loads (x-axis in mN) calculated by the energy method; (b) correlation between K_c and H/E for both minerals.

Both minerals exhibit significant standard deviation in K_c, reflecting strong microscale heterogeneity, consistent with earlier studies showing that microcracks, pore distributions, and impurity phases substantially influence fracture behavior in phyllosilicate-rich materials (Eberhardt et al., 1998; Gupta et al., 2020). For ripidolite, mean K_c generally increases with increasing peak load, although a slight reduction is observed at 160 mN. This trend suggests that higher loads create larger fracture process zones, which engage more grain boundaries and interlayer regions capable of absorbing energy before crack propagation, thereby enhancing the apparent toughness. Similar mechanisms, in which the size of the plastic zone influences indentation fracture toughness, are well documented in the indentation literature (Feng and Zhang, 2015). In contrast, illite shows no clear trend in K_c with load, which may reflect its structurally rigid nature and reinforcing mineral inclusions such as quartz, resulting in a fracture response less sensitive to load variation.

At most peak loads, ripidolite shows higher K_c values than illite. For instance, at 60 mN, the mean K_c for ripidolite and illite are 0.68 and 0.54 MPa·m$^{0.5}$, respectively. This disparity may stem from the greater capacity of ripidolite for localized plastic deformation, which dissipates more energy prior to fracture. Illite's greater brittleness and limited plasticity likely facilitate earlier crack initiation with less energy absorption. Such behavior aligns with

observations in brittle materials where plastic work near the crack tip affects toughness measured via indentation (Zhao et al., 2021).

As shown in Fig. 8 (b), both minerals present a negative correlation between K_c and H/E, with a particularly strong linear relationship in ripidolite. This can be explained by the way indentation work is partitioned into elastic storage and plastic dissipation. A higher H/E ratio indicates that the material stores more of the applied energy elastically and allows less plastic flow. When a crack initiates, the stored elastic energy is released and drives crack propagation, which lowers the apparent fracture toughness. Conversely, a lower H/E ratio reflects greater plastic accommodation during indentation. In this case, more of the applied energy is dissipated in plastic deformation near the crack tip, which shields the crack and delays its growth, leading to higher fracture toughness. The stronger correlation observed in ripidolite implies that its toughness is closely controlled by the balance between elastic storage and plastic dissipation, where illite's weaker correlation suggests that its fracture resistance is influenced more by microstructural factors such as quartz inclusions and inherent brittleness. Such negative correlations between K_c and H/E have been reported in rocks and ceramics (Datye et al., 2018; Gupta et al., 2020).

4.3.Creep behavior

During the holding segment of the nanoindentation process, creep displacement as a function of time can be extracted directly. Fig. 9 presents representative creep displacement-time curves for ripidolite and illite under various loading conditions, where the initial displacement and time are normalized to zero to facilitate direct comparison between minerals. Across all test conditions, the dispersion of creep curves is visibly smaller in illite than in ripidolite, indicating its uniformly mechanical response. By contrast, ripidolite shows a wider spread of creep curves, reflecting its time-dependent deformation may be strongly influenced by microstructural heterogeneity, particularly the presence of pores.

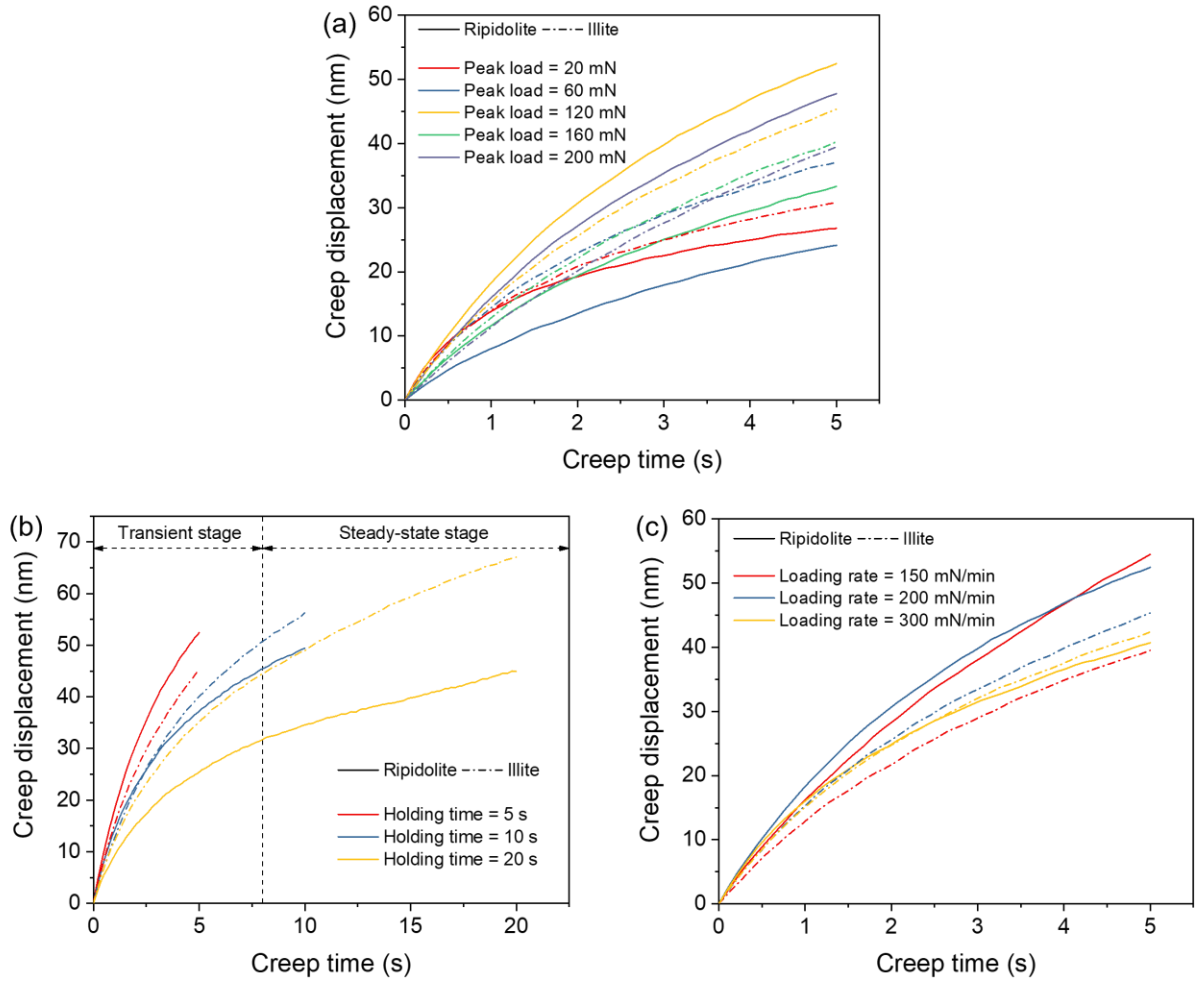

Fig. 9 Creep displacement-time curves for ripidolite and illite under (a) peak loads, (b) holding times, and (c) loading rates.

As shown in Fig. 9 (b), the creep process of both minerals comprises two stages: an initial transient stage and a steady-state stage, in agreement with previous nanoindentation studies on geomaterials (Ma et al., 2022; Sun et al., 2020). The transition occurs at around 8 s, where the transient stage shows a progressively decreasing creep rate associated with rapid compaction, followed by a steady-state stage with an approximately constant creep rate. This behavior is also evident from the progressively reduced slopes of the curves in Fig. 9 (a) and (c). The transient stage corresponds to the rapid rearrangement and bending of layered clay structures, whereas the steady-state stage reflects slower viscoplastic processes such as interlayer slip and intergranular accommodation.

To quantify the creep response, the indentation creep ratio (C_{IT}) was calculated using Eq. (16), where a higher value indicates greater time-dependent deformation (Wang et al., 2022b; Zhang et al., 2024).

$$C_{IT} = \frac{h_m - h_l}{h_l} \times 100\% \tag{16}$$

Fig. 10 summarizes C_{IT} values for ripidolite and illite under different loading conditions. Across nearly all conditions, the standard deviation in illite is smaller than that in ripidolite, confirming the visual observations from Fig. 9. Moreover, illite generally exhibits higher mean C_{IT} than ripidolite under the same test conditions, despite having higher hardness and elastic modulus. This apparent contradiction arises from the smaller h_l values in illite during nanoindentation, which amplify the relative creep displacement in Eq. (16), and from microstructural factors such as the presence of harder impurity phases (e.g., quartz) that concentrate local stresses and promote time-dependent deformation via microcracking and interlayer slip (Wang et al., 2022a).

In Fig. 10 (a), both minerals show a systematic decrease in creep ratio with increasing peak load, for example, the mean C_{IT} decreases from 2.24 % to 1.17 % in ripidolite and from 2.81 % to 1.44 % in illite as the peak load increases from 20 mN to 200 mN. This can be explained by the increased h_l at higher peak loads, which reduces the normalized contribution of creep displacement, and by the densification of the subsurface microstructure during initial loading, which limits subsequent time-dependent deformation (Charlton et al., 2023). In Fig. 10 (b), ripidolite shows insignificant change in C_{IT} with holding time, while illite displays an increase in C_{IT} with prolonged holding, indicating enhanced creep deformation over longer periods. This suggests that time-dependent damage mechanisms in illite, such as interlayer sliding and crack extension, are more active during sustained loading (Ma et al., 2025). In Fig. 10 (c), neither mineral shows a clear monotonic trend with loading rate, but both reach their highest C_{IT} at 200 mN/min. This suggests that creep reflects a balance between competing processes: slower

rates allow stress to relax during loading, reducing creep, while very fast rates drive mainly plastic penetration with limited time-dependent strain. At intermediate rates, elastic energy storage and relaxation both contribute, enhancing creep, consistent with rate-sensitive behavior observed in other geological materials (Wang et al., 2022b).

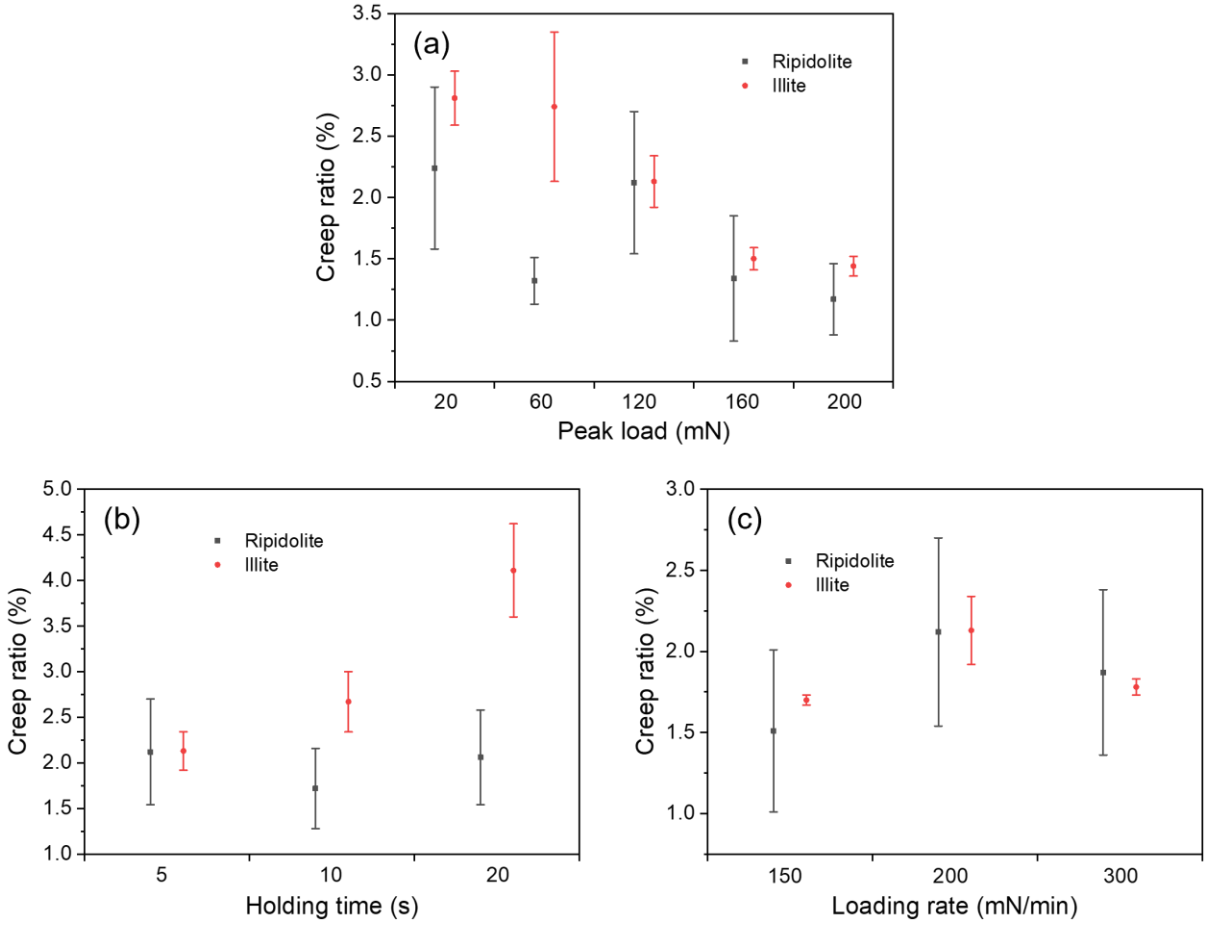

Fig. 10 Indentation creep ratio of ripidolite and illite under (a) peak loads, (b) holding times, and (c) loading rates.

4.4.Implications and limitations

The combined trends in hardness, elastic modulus, fracture toughness, and creep behavior provide an integrated view of how ripidolite and illite control fluid pathways and contribute to caprock integrity. Illite's higher hardness and elastic modulus indicate superior resistance to short-term deformation, but its generally lower fracture toughness makes it more prone to brittle cracking, which could generate new microfractures and increase leakage risk under stress concentrations. In contrast, ripidolite generally shows higher fracture toughness and thus

a greater ability to dissipate energy before crack propagation. Its softer response and relatively lower modulus promote localized compaction, which may close pore spaces and reduce permeability, though near-well deformation could still weaken seal locally.

Creep results add a time-dependent dimension to these observations. Illite's higher creep ratios indicate greater susceptibility to long-term viscoelastic or viscoplastic strain, which could widen existing pores and microcracks, compromising sealing efficiency over extended storage periods. Ripidolite's lower creep ratios point to greater dimensional stability under constant stress, though its tendency for immediate plastic deformation still raises risks of compaction around injection zones.

In real subsurface settings, additional factors such as high temperature, elevated pore pressure, and brine-mineral interactions further alter both fracture and creep mechanisms (Wang et al., 2021). The short holding times in this study limit direct extrapolation to geological timescales. Future work should therefore include extended creep tests under subsurface-simulated conditions to capture long-term responses. Additionally, seasonal hydrogen or hydrocarbon storage involves cyclic injection and withdrawal, which subjects caprocks to repeated loading-unloading sequences. Such cycles may induce fatigue damage and accelerate crack growth (Naderloo et al., 2023), particularly in minerals with lower fracture toughness. Understanding how mineral-scale deformation influences pore networks and fluid pathways is thus essential for accurately predicting caprock performance in underground energy storage operations.

5. Conclusions

This study applied systematic nanoindentation tests to ripidolite and illite under varying peak loads, holding times, and loading rates, focusing on hardness, elastic modulus, fracture toughness, and creep behavior. The key findings are:

1) Ripidolite frequently exhibited pop-in events during loading, reflecting localized plasticity triggered by pores and microstructural heterogeneity. Illite showed smoother loading curves and consistently smaller indentation depths, confirming its greater resistance to penetration.
2) Microscopy revealed distinct deformation mechanisms. Ripidolite deformed primarily though pile-up without visible cracking, whereas illite displayed limited pile-up but radial and lateral cracks at higher loads. These contrasts highlighted ripidolite's tendency for plastic flow around the indent and illite's propensity for brittle fracture.
3) Illite consistently showed higher hardness and elastic modulus, indicating its stiffer structure and harder mineral inclusions. Ripidolite, however, presented a stronger indentation size effect in hardness and generally higher fracture toughness, suggesting its greater ability to dissipate energy before crack propagation.
4) Both minerals followed a two-stage creep response comprising a transient and a steady-state stage. Illite generally showed higher creep ratios, implying greater susceptibility to time-dependent strain despite its higher strength. Ripidolite's lower creep ratios indicated better dimensional stability under sustained load but greater susceptibility to immediate plastic deformation.

Overall, illite offers superior resistance to short-term deformation but is more prone to brittle cracking and time-dependent strain, whereas ripidolite better resists crack propagation but undergoes greater plastic deformation under load. These contrasting behaviors underscores the importance of considering mineral-scale responses when evaluating the sealing capacity of clay-rich caprocks in subsurface energy storage applications.

Declaration of competing interest

The authors declare that they have no known competing financial interests or personal relationships that could have appeared to influence the work reported in this paper.

Acknowledgements

The first author gratefully acknowledges the financial support provided by the China Scholarship Council. This work was also financially supported by the Chongqing Science and Technology Bureau Foundation (CSTB2023NSCQ-MSX0560). The authors would like to thank Mr. Sander Huisman for his professional assistance with polishing the clay samples.

References

Bartier, D. and Auvray, C. [2017] Determination of elastic modulus of claystone: Nano-/micro-indentation and meso-compression tests used to investigate impact of alkaline fluid propagation over 18 years. *Journal of Rock Mechanics and Geotechnical Engineering*, **9**(3), 511-518.

Bennett, K.C., Berla, L.A., Nix, W.D. and Borja, R.I. [2015] Instrumented nanoindentation and 3D mechanistic modeling of a shale at multiple scales. *Acta Geotechnica*, **10**(1), 1-14.

Charlton, T., Rouainia, M., Aplin, A., Fisher, Q. and Bowen, L. [2023] Nanoindentation of Horn River Basin shales: The micromechanical contrast between overburden and reservoir formations. *Journal of Geophysical Research: Solid Earth*, **128**(3), e2022JB025957.

Chen, X., Hutchinson, J.W. and Evans, A.G. [2005] The mechanics of indentation induced lateral cracking. *Journal of the American Ceramic Society*, **88**(5), 1233-1238.

Cheng, P., Zhang, C.P., Ma, Z.Y., Zhou, J.P., Zhang, D.C., Liu, X.F., Chen, H. and Ranjith, P.G. [2022] Experimental study of micromechanical properties alterations of shale matrix treated by $ScCO_2$-water saturation using nanoindentation tests. *Energy*, **242**.

Cheng, Y.-T., Li, Z. and Cheng, C.-M. [2002] Scaling relationships for indentation measurements. *Philosophical Magazine A*, **82**(10), 1821-1829.

Chudoba, T. and Richter, F. [2001] Investigation of creep behaviour under load during indentation experiments and its influence on hardness and modulus results. *Surface and Coatings Technology*, **148**(2), 191-198.

Ciancimino, A., Cosentini, R.M., Foti, S., Messori, A., Ullah, H., Volonté, G. and Musso, G. [2024] A preliminary investigation on the mechanical behaviour of a stiff Italian clay in the context of hydrogen storage. *Geomechanics for Energy and the Environment*, **38**.

Cosenza, P., Giot, R. and Hedan, S. [2023] Elastic moduli of clay minerals and their aggregates: A review. *Applied Clay Science*, **236**.

Datye, A., Schwarz, U. and Lin, H.-T. [2018] Fracture toughness evaluation and plastic behavior law of a single crystal silicon carbide by nanoindentation. *Ceramics*, **1**(1), 198-210.

Dilshan, R.A.D.P., Perera, M.S.A. and Matthai, S.K. [2024] Effect of mechanical weakening and crack formation on caprock integrity during underground hydrogen storage in depleted gas reservoirs – A comprehensive review. *Fuel*, **371**.

Dje, L.B. and Radonjic, M. [2025] Reactivity of shale to supercritical CO_2: Insights from microstructural characterization and mineral phase evolution in Caney shales for CCUS applications. *Materials*, **18**(14), 3382.

Domnich, V., Gogotsi, Y. and Dub, S. [2000] Effect of phase transformations on the shape of the unloading curve in the nanoindentation of silicon. *Applied Physics Letters*, **76**(16), 2214-2216.

Eberhardt, E., Stead, D., Stimpson, B. and Read, R. [1998] Identifying crack initiation and propagation thresholds in brittle rock. *Canadian Geotechnical Journal*, **35**(2), 222-233.

Elmi, C. [2023] Physical-chemical properties of nano-sized phyllosilicates: Recent environmental and industrial advancements. *Encyclopedia*, **3**(4), 1439-1460.

Feng, Y. and Zhang, T. [2015] Determination of fracture toughness of brittle materials by indentation. *Acta Mechanica Solida Sinica*, **28**(3), 221-234.

Fischer-Cripps, A.C., 2007. Depth-sensing indentation testing. In: A.C. Fischer-Cripps (Editor), Introduction to Contact Mechanics. Springer US, Boston, MA, pp. 189-199.

Gailhanou, H., van Miltenburg, J.C., Rogez, J., Olives, J., Amouric, M., Gaucher, E.C. and Blanc, P. [2007] Thermodynamic properties of anhydrous smectite MX-80, illite IMt-2 and mixed-layer illite–smectite ISCz-1 as determined by calorimetric methods. Part I: Heat capacities, heat contents and entropies. *Geochimica et Cosmochimica Acta*, **71**(22), 5463-5473.

Gupta, I., Sondergeld, C. and Rai, C. [2020] Fracture toughness in shales using nano-indentation. *Journal of Petroleum Science and Engineering*, **191**.

Konta, J. [2009] Phyllosilicates in the sediment-forming processes: weathering, erosion, transportation, and deposition. *Acta Geodynamica et Geomaterialia*, **6**(1), 13.

Kulshreshtha, P.K., Youssef, K.M. and Rozgonyi, G. [2012] Nano-indentation: A tool to investigate crack propagation related phase transitions in PV silicon. *Solar Energy Materials and Solar Cells*, **96**, 166-172.

Liu, K., Ostadhassan, M. and Bubach, B. [2016] Applications of nano-indentation methods to estimate nanoscale mechanical properties of shale reservoir rocks. *Journal of Natural Gas Science and Engineering*, **35**, 1310-1319.

Ma, H., Fan, P., Qian, Q., Zhang, Q., Li, K., Zhu, S. and Yuan, D. [2024] Nanoindentation test of ion-irradiated materials: Issues, modeling and challenges. *Materials (Basel)*, **17**(13).

Ma, X., Higgins, W., Liang, Z., Zhao, D., Pharr, G.M. and Xie, K.Y. [2021] Exploring the origins of the indentation size effect at submicron scales. *Proceedings of the National Academy of Sciences*, **118**(30), e2025657118.

Ma, Z., Zhang, C., Pathegama Gamage, R. and Zhang, G. [2022] Uncovering the creep deformation mechanism of rock-forming minerals using nanoindentation. *International Journal of Mining Science and Technology*, **32**(2), 283-294.

Ma, Z., Zhou, L., Zuo, S., Kang, X. and Zhang, J. [2025] Rheological properties of red shale mineral components by nanoindentation experiment. *Geomechanics and Geophysics for Geo-Energy and Geo-Resources*, **11**(1).

Mishra, T., de Rooij, M., Shisode, M., Hazrati, J. and Schipper, D.J. [2020] Characterization of yield criteria for zinc coated steel sheets using nano-indentation with knoop indenter. *Surface and Coatings Technology*, **381**.

Mu, Y., Zou, C., Hu, Z., Pan, S., Duan, X., Gao, Y. and Tang, Y. [2024] Hydrogen-water-rock interaction from the perspective of underground hydrogen storage: Micromechanical properties and mineral content of rock. *International Journal of Hydrogen Energy*, **70**, 79-90.

Mukherjee, R. and Misra, S. [2023] Nanomechanics of minerals: understandings and developments through instrumented nanoindentation techniques. *Physics and Chemistry of Minerals*, **50**(1).

Naderloo, M., Ramesh Kumar, K., Hernandez, E., Hajibeygi, H. and Barnhoorn, A. [2023] Experimental and numerical investigation of sandstone deformation under cycling loading relevant for underground energy storage. *Journal of Energy Storage*, **64**.

Ohmura, T. and Wakeda, M. [2021] Pop-in phenomenon as a fundamental plasticity probed by nanoindentation technique. *Materials (Basel)*, **14**(8).

Oliver, W.C. and Pharr, G.M. [1992] An improved technique for determining hardness and elastic modulus using load and displacement sensing indentation experiments. *Journal of Materials Research*, **7**(06), 1564-1583.

Pauling, L. [1930] The structure of the chlorites. *Proceedings of the National Academy of Sciences*, **16**(9), 578-582.

Poda, S. and Talal, G. [2025] Geomechanical and geochemical considerations for hydrogen storage in shale and tight reservoirs. *Processes*, **13**(8), 2522.

Shi, X., Misch, D., Zak, S., Cordill, M. and Kiener, D. [2024] Mapping the composite nature of clay matrix in mudstones: integrated micromechanics profiling by high-throughput nanoindentation and data analysis. *Geomechanics and Geophysics for Geo-Energy and Geo-Resources*, **10**(1), 139.

Stixrude, L. and Peacor, D.R. [2002] First-principles study of illite–smectite and implications for clay mineral systems. *Nature*, **420**(6912), 165-168.

Sun, C., Li, G., Gomah, M.E., Xu, J. and Sun, Y. [2020] Creep characteristics of coal and rock investigated by nanoindentation. *International Journal of Mining Science and Technology*, **30**(6), 769-776.

Vogt, C., Lauterjung, J.r. and Fischer, R.X. [2002] Investigation of the clay fraction (< 2 μm) of the clay minerals society reference clays. *Clays and Clay Minerals*, **50**(3), 388-400.

Wang, J., Liu, Y., Yang, C., Jiang, W., Li, Y., Xiong, Y. and Wu, B. [2022a] Modeling the viscoelastic behavior of quartz and clay minerals in shale by nanoindentation creep tests. *Geofluids*, **2022**, 1-16.

Wang, J., Liu, Y., Yang, C., Zheng, Y., Jiang, W., Menegon, L., Renard, F., Peng, P.a. and Xiong, Y. [2023] Upscaling the creep behavior of clay-rich and quartz-rich shales from nanoindentation measurements: Application to the Wufeng-Longmaxi shale, China. *International Journal of Rock Mechanics and Mining Sciences*, **171**.

Wang, J., Yang, C., Liu, Y., Li, Y. and Xiong, Y. [2022b] Using nanoindentation to characterize the mechanical and creep properties of shale: Load and loading strain rate effects. *ACS Omega*, **7**(16), 14317-14331.

Wang, Y., Porter, D.L., Naleway, S.E. and Newell, P. [2021] Thermo-mechanical characterization of shale using nanoindentation. *Scientific Reports*, **11**(1), 18864.

Wethington, C., Pashin, J., Wethington, J., Esposito, R. and Riestenberg, D. [2022] Mudstone baffles and barriers in lower cretaceous strata at a proposed CO_2 storage hub in Kemper County, Mississippi, United States. *Frontiers in Energy Research*, **10**, 904850.

Yang, G., Ma, X., Feng, T., Yu, Y., Yin, S., Huang, M. and Wang, Y. [2020] Geochemical modelling of the evolution of caprock sealing capacity at the Shenhua CCS demonstration project. *Minerals*, **10**(11), 1009.
Zeng, Q., Feng, Y. and Xu, S. [2017] A discussion of "Application of nano-indentation methods to estimate nanoscale mechanical properties of shale reservoir rocks" by K Liu, M Osatadhassan and B Bubach. *Journal of Natural Gas Science and Engineering*, **42**, 187-189.
Zhang, J., Hu, L., Pant, R., Yu, Y., Wei, Z. and Zhang, G. [2013] Effects of interlayer interactions on the nanoindentation behavior and hardness of 2:1 phyllosilicates. *Applied Clay Science*, **80-81**, 267-280.
Zhang, P., Zhang, D. and Zhao, J. [2024] Control of fracture toughness of kerogen on artificially-matured shale samples: An energy-based nanoindentation analysis. *Gas Science and Engineering*, **124**.
Zhao, L., Zhang, J., Pfetzing, J., Alam, M. and Hartmaier, A. [2021] Depth-sensing ductile and brittle deformation in 3C-SiC under Berkovich nanoindentation. *Materials & Design*, **197**, 109223.